ACS APPLIED MATERIALS & INTERFACES

Letter

Cite This: ACS Appl. Mater. Interfaces XXXX, XXX, XXX−XXX

www.acsami.org

Suppression of Monoclinic Phase Transitions of O3-Type Cathodes Based on Electronic Delocalization for Na-Ion Batteries

Hu-Rong Yao,[†,‡,∥] Wei-Jun Lv,[†,∥] Ya-Xia Yin,[‡,⊥] Huan Ye,[‡] Xiong-Wei Wu,[‡] Yi Wang,[§,⊥] Yue Gong,[§,⊥] Qinghao Li,[§,⊥] Xiqian Yu,[§,⊥] Lin Gu,[§,⊥] Zhigao Huang,*[,†,∥] and Yu-Guo Guo*[,‡,⊥]

[†]Fujian Provincial Key Laboratory of Quantum Manipulation and New Energy Materials College of Physics and Energy, Fujian Normal University, Fuzhou 350117, China

[‡]CAS Key Laboratory of Molecular Nanostructure and Nanotechnology, CAS Research/Education Center for Excellence in Molecular Sciences, Beijing National Laboratory for Molecular Sciences (BNLMS), Institute of Chemistry, and [§]Beijing National Laboratory for Condensed Matter Physics, Institute of Physics, Chinese Academy of Sciences (CAS), Beijing 100190, P. R. China

[∥]Fujian Provincial Collaborative Innovation Center for Optoelectronic Semiconductors and Efficient Devices, Xiamen, 361005, China

[⊥]University of Chinese Academy of Sciences, Beijing 100049, China

Supporting Information

ABSTRACT: As high capacity cathodes, O3-type Na-based oxides always suffer from a series of monoclinic transitions upon sodiation/desodiation, mainly caused by Na^+/vacancy ordering and Jahn−Teller (J−T) distortion, leading to rapid structural degradation and serious performance fading. Herein, a simple modulation strategy is proposed to address this issue based on refrainment of electron localization in expectation to alleviate the charge ordering and change of electronic structure, which always lead to Na^+/vacancy ordering and J−T distortion, respectively. According to density functional theory calculations, Fe^{3+} with slightly larger radius is introduced into $NaNi_{0.5}Mn_{0.5}O_2$ with the intention of enlarging transition metal layers and facilitating electronic delocalization. The obtained $NaFe_{0.3}Ni_{0.35}Mn_{0.35}O_2$ exhibits a reversible phase transition of $O3_{hex}$−$P3_{hex}$ without any monoclinic transitions in striking contrast with the complicated phase transitions ($O3_{hex}$−$O'3_{mon}$−$P3_{hex}$−$P'3_{mon}$−$P3'_{hex}$) of $NaNi_{0.5}Mn_{0.5}O_2$, thus excellently improving the capacity retention with a high rate kinetic. In addition, the strategy is also effective to enhance the air stability, proved by direct observation of atomic-scale ABF-STEM for the first time.

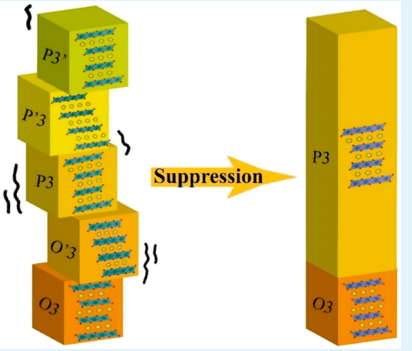

KEYWORDS: *Na-ion batteries, cathode materials, monoclinic phase transitions, electronic delocalization, electrochemical properties*

Li-ion batteries (LIBs) have got resounding success in the portable electronics and are expected to power electric vehicles owing to their high energy density.[1−4] Nevertheless, the sharply increased demand for LIBs is in contradiction with the scarce abundance of Li.[5−8] In this context, Na-ion batteries (NIBs) exhibit intrinsic advantages compared to their LIB counterparts owing to the high availability and low cost of Na resources, especially for the applications in large-scale energy storage devices.[9−13] The huge utilization potentiality of NIBs motivates extensive researches on various Na-based cathodes, in which O3-type transition metal oxides ($NaTmO_2$) are recognized as one of promising materials.[14] $NaTmO_2$, in which octahedrally coordinated active ions and transition metal ions are alternately accommodated in the cubic close-packed oxygen columns, has a similar structure to Li counterparts $LiCoO_2$ and is expected to follow the successful use of $LiCoO_2$ in LIBs.[15,16] However, their practical application is limited by the low Na diffusion rate and poor cycling performance resulting from the much more complicated phase transitions upon sodiation/desodiation. During charging/discharging, the structure of $NaTmO_2$ always undergoes multiple monoclinic phases mainly caused by the Na^+/vacancy ordering and J−T effects of active transition metal ions.[17−20] As reported, The $NaNiO_2$ predicts four monoclinic transitions of O′3−P′3 − P″3 − O″3−O‴3 when charged from 1.5 to 4.0 V, exhibiting a poor capacity retention of 82% after 25 cycles.[21,22] Doping various metal elements into transition metal layers has been proven effective at suppressing the complicated phase transition and thus improving the electrochemical properties.[23−26] However, the mechanism of how dopant mediates the distortion remains unclear, and the strategic doping to suppress monoclinic transitions has rarely been studied.

In this work, considering Na^+/vacancy ordering and J−T distortion of $NaTmO_2$ mainly originates from the change of localized electronic structure upon sodiation/desodiation, an effective design strategy is suggested to suppress the

Received: January 4, 2019
Accepted: April 23, 2019
Published: April 23, 2019

DOI: 10.1021/acsami.9b00186
ACS Appl. Mater. Interfaces XXXX, XXX, XXX−XXX

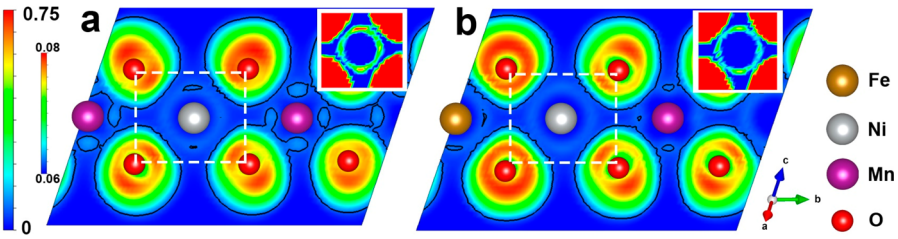

Figure 1. ELF slices alone the (106) plane of (a) $NaNi_{0.5}Mn_{0.5}O_2$ and (b) $NaFe_{0.3}Ni_{0.35}Mn_{0.35}O_2$. Insets of a and b correspond to the increasing ELFs around the white-rectangle-marked Ni ion. The ELF values of 0.15 are indicated as black lines.

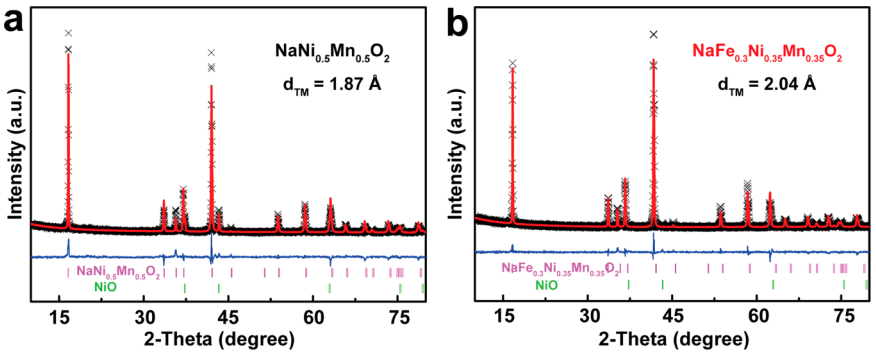

Figure 2. Powder XRD profiles and Rietveld refinement patterns for (a) $NaNi_{0.5}Mn_{0.5}O_2$ and (b) $NaFe_{0.3}Ni_{0.35}Mn_{0.35}O_2$.

monoclinic transitions via refraining the electron localization around transition metal ions. On the basis of density functional theory (DFT) calculations, we successfully modulate the electronic structure via introducing heteroatom with a slightly larger radius in expectation to ensure a homogeneous incorporation and simultaneously enlarge transition metal layers thus to intensify the degree of electronic delocalization, well verified by the modulation on $NaNi_{0.5}Mn_{0.5}O_2$ via Fe substitution. The obtained $NaFe_{0.3}Ni_{0.35}Mn_{0.35}O_2$ does not show any monoclinic phases throughout whole charging process. This is in sharp contrast to two monoclinic phases $O'3_{mon}$ and $P'3_{mon}$ for the original $NaNi_{0.5}Mn_{0.5}O_2$, implied by the analysis of in situ X-ray diffraction (XRD). The difference results in an optimal electrochemical performances based on complete reversibility of double redox couples (Ni^{2+}/Ni^{3+} and Fe^{3+}/Fe^{4+}) investigated by ex situ X-ray absorption near-edge structure (XANES) spectra. Furthermore, air stability of material is also excellently improved, directly verified by annular bright-field (ABF) STEM at atomic resolution for the first time.

First, we carry out DFT calculations to reveal the impacts of incorporated Fe^{3+} on crystal and electronic structure to verify feasibility of the strategy mentioned above. It is obvious that Fe doping leads to the expansion of transition metal layers as a result of slightly larger radius of high spin-polarization Fe^{3+} (64.5 pm) than the average value (61.0 pm) of high spin-polarization Ni^{2+} and Mn^{4+} (Figure S1),[27] which is also consistent with the powder XRD refinement results discussed below. Furthermore, the degree of electronic localization around transition metal ions in $NaNi_{0.5}Mn_{0.5}O_2$ and $NaFe_{0.3}Ni_{0.35}Mn_{0.35}O_2$ are compared by the electronic localization functions (ELF) calculations.[28] As shown in Figure 1, the two-dimensional ELF slice along (106) surface comprises between 0 and 0.75, in which the bigger ELF value indicates the stronger localization of electron.[29,30] To enable a visual comparison, the contour lines for ELF = 0.15 are also displayed. It is obvious that the degree of electron localization around transition metal ions is significantly refrained upon Fe substitution because of the expansion of TmO_2 layers. Considering the main effect of Ni^{3+} with J−T distortion to monoclinic transitions,[31] the ELFs around Ni (insets) are shown in more detailed comparison from 0.06 to 0.08, clearly indicating the stronger electron delocalization of $NaFe_{0.3}Ni_{0.35}Mn_{0.35}O_2$. The results of DFT calculations imply modulation on the microstructure of $NaNi_{0.5}Mn_{0.5}O_2$, expansion of TmO_2 layer spacing, and refrainment of electron localization, is accessible via Fe^{3+} substitution with a slightly larger radius.

Based on the calculated results discussed above, we prepare the $NaFe_xNi_{0.5-x/2}Mn_{0.5-x/2}O_2$ (x = 0, 0.3) samples by high-temperature solid-state method. The morphology of $NaFe_{0.3}Ni_{0.35}Mn_{0.35}O_2$ with particle size of approximately 2 to 5 μm (Figure S2) is observed by scanning electron microscopy (SEM). As shown in energy dispersive spectroscopy (EDS) elementary mappings (Figure S3), Na, Fe, Ni, Mn, and O are uniformly distributed in the particle of prepared $NaFe_{0.3}Ni_{0.35}Mn_{0.35}O_2$. The collected powder XRD patterns shown in Figure 2 reveal that Fe doping maintains original $R\bar{3}m$ hexagonal lattice with α-$NaFeO_2$ stacking structure, except for a trace amount of NiO impurity.[32] The corresponding Rietveld refined crystallographic data (Tables S1 and S2) show that the Fe, Ni, and Mn ions occupy 3*b* Wyckoff sites, identical to the expected design of a uniform substitution of Fe^{3+} in transition metal layers. The distance of TmO_2 layers of $NaFe_{0.3}Ni_{0.35}Mn_{0.35}O_2$ (2.04 Å) distinctly increase in comparison to 1.87 Å of original $NaNi_{0.5}Mn_{0.5}O_2$, well consistent with the results of DFT calculations.

Following the successful structure design of $NaFe_{0.3}Ni_{0.35}Mn_{0.35}O_2$, the Na storage performances are examined by galvanostatic charge/discharge test and cyclic voltammogram (CV) in Na half-cells over 2.0−4.0 V voltage range. The charge/discharge profiles (Figure 3a) of Fe free $NaNi_{0.5}Mn_{0.5}O_2$ exhibits several voltage plateaus, corresponding to a series of complicated phase transitions of $O3_{hex}$−$O'3_{mon}$−

DOI: 10.1021/acsami.9b00186
ACS Appl. Mater. Interfaces XXXX, XXX, XXX−XXX

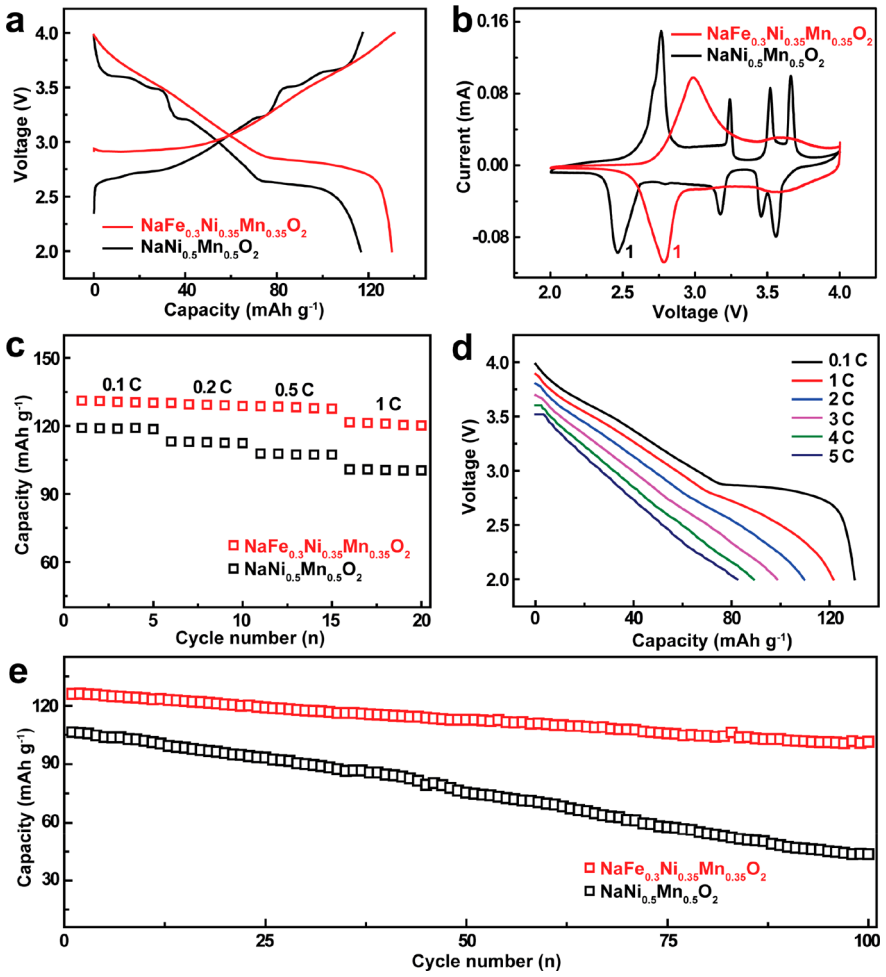

Figure 3. (a) Charge/discharge profiles of $NaNi_{0.5}Mn_{0.5}O_2$ and $NaFe_{0.3}Ni_{0.35}Mn_{0.35}O_2$ at the first cycle tested at 0.1*C*. (b) CV curves tested at scanning rate of 0.05 mV s^{-1} within 2.0−4.0 V voltage range. (c) Corresponding rate performances. (d) Discharge profiles of $NaFe_{0.3}Ni_{0.35}Mn_{0.35}O_2$ at various rates. (e) Cyclic performances at current rate of 1*C*.

$P3_{hex}$−$P'3_{mon}$−$P3'_{hex}$ (Figure S4) originating from the gliding of TmO_2 layers and structure distortion.[33] By comparison, $NaFe_{0.3}Ni_{0.35}Mn_{0.35}O_2$ displays a much smoother charge/discharge curve, a plateau around 2.8−2.9 V and a completely sloping profile above 3.0 V, corresponding to the phase transition of $O3_{hex}$−$P3_{hex}$ and a large solid-solution region discussed in the later section. In addition, Fe substitution leads to a higher capacity of 130.3 mAh g^{-1} (116.7 mAh g^{-1} of $NaNi_{0.5}Mn_{0.5}O_2$) and a higher average voltage of 3.11 V (2.98 V of $NaNi_{0.5}Mn_{0.5}O_2$). The CV curves of pristine materials tested at 0.05 mV s^{-1} are compared as displayed in Figure 3b. In comparison with the four distinguishable oxidation/reduction peaks of $NaNi_{0.5}Mn_{0.5}O_2$, the major CV feature of $NaFe_{0.3}Ni_{0.35}Mn_{0.35}O_2$ is only one peak in correspondence with the charge/discharge measurement results. The oxidation/reduction peaks marked by "1" are chosen to compare polarizability. The polarization of $NaFe_{0.3}Ni_{0.35}Mn_{0.35}O_2$ (204 mV) is much smaller than that of $NaNi_{0.5}Mn_{0.5}O_2$ (296 mV), in good agreement with the improved rate performance. Benefiting from the suppression of monoclinic phase transitions and the large solid-solution region, $NaFe_{0.3}Ni_{0.35}Mn_{0.35}O_2$ exhibits excellent rate performance (Figure 3c). $NaFe_{0.3}Ni_{0.35}Mn_{0.35}O_2$ still preserves a specific capacity of 82.3 mAh g^{-1} (more than 63% of capacity at 0.1*C*) even with the 5*C* rate shown in Figure 3d. Also, the effect of the strategy on improvement of cyclability is proved by the cyclic test at 1*C*. As shown in Figure S5, the crystal structure of $NaNi_{0.5}Mn_{0.5}O_2$ cannot completely recover back to initial O3-phase after cycling 10 times, which leads to a rapid fade of capacity. Comparatively, $NaFe_{0.3}Ni_{0.35}Mn_{0.35}O_2$ (Figure 3e) demonstrates its optimized cyclability by a doubled capacity retention increase after 100 cycles (80% of $NaFe_{0.3}Ni_{0.35}Mn_{0.35}O_2$ and 41% of $NaNi_{0.5}Mn_{0.5}O_2$). These results show that Fe substitution into the transition-metal layers of $NaNi_{0.5}Mn_{0.5}O_2$ represents an improved Na storage behavior in terms of capacity, average voltage, energy density, rate, and cycling performance.

To grasp the detailed mechanism under optimized electrochemical performances and testify the effect of modulation strategy, we carry out the structural evolution of $NaFe_{0.3}Ni_{0.35}Mn_{0.35}O_2$ compounds during sodiation/desodiation over a 2.0−4.0 V voltage range by in situ XRD measurement along with the first charge/discharge cycle (Figure 4a). The asterisks and pounds represent the diffraction peaks of NiO (impurity) and Al (current collector and X-ray window), respectively. Upon initial charge, the sample structure experiences a monophasic reaction indicated by all peaks being indexed to the hexagonal O3 phase. Upon further Na extraction, the new diffraction peaks indexed to hexagonal P3 phase are found with the coexistence of the O3 phase through

DOI: 10.1021/acsami.9b00186
ACS Appl. Mater. Interfaces XXXX, XXX, XXX−XXX

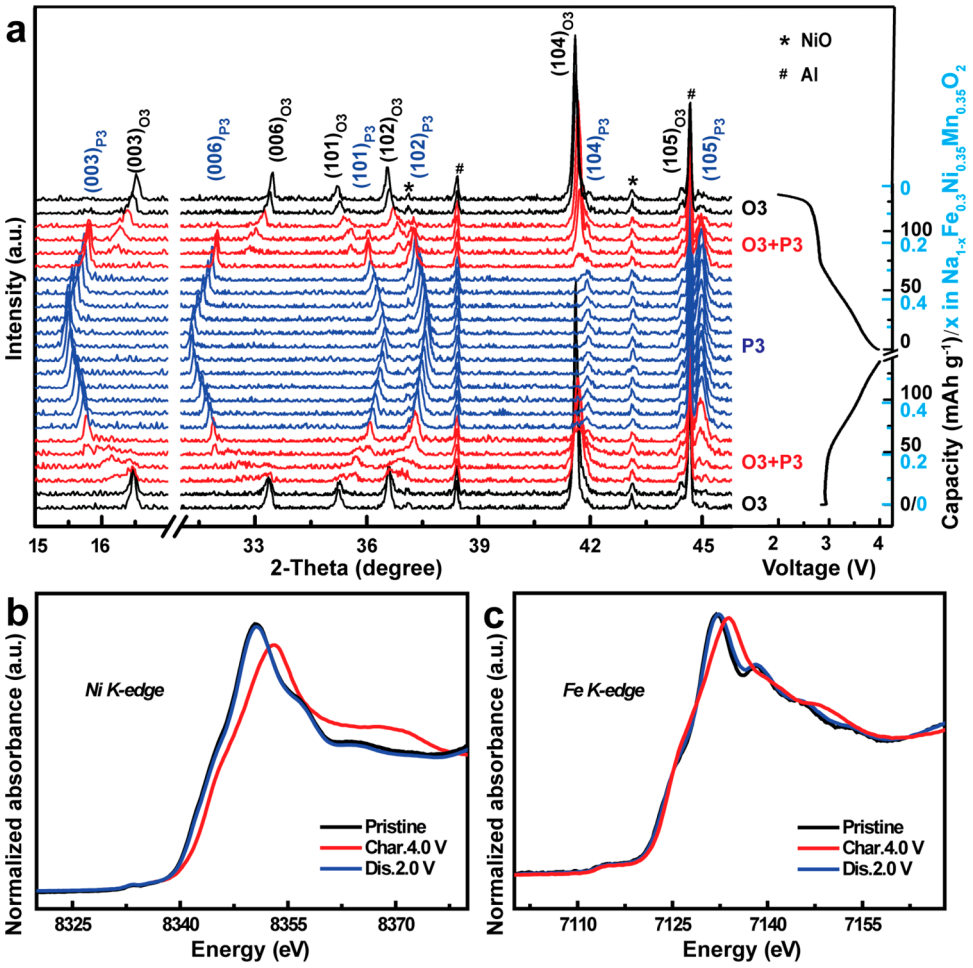

Figure 4. (a) In situ XRD patterns of $NaFe_{0.3}Ni_{0.35}Mn_{0.35}O_2$ tested within 2.0−4.0 V, in which the black and blue scales (right) represent capacity and corresponding x value in $Na_{1-x}Fe_{0.3}Ni_{0.35}Mn_{0.35}O_2$, respectively. Ex situ XANES spectra at (b) Ni *K*-edge and (c) Fe *K*-edge of $NaFe_{0.3}Ni_{0.35}Mn_{0.35}O_2$ recorded under various electrochemical states.

the $O3_{hex}$−$P3_{hex}$ phase transition, responsible for the long voltage plateau of around 2.8 V. With the completion of the transition from O3 to P3, the (003) and (006) of P3 diffraction peaks continuously shift toward a lower angle without any new phases until the end of charged to 4.0 V, implying a large solid-solution region consistent with the sloping profiles above 3.0 V, with a gradually expanded interlayer distance due to the decreased electrostatic shielding upon desodiation. Upon the reverse discharge, an opposite evolution is exhibited and a set of well-defined O3 phase peaks are recovered to the original position when discharged to 2.0 V, indicating the high reversibility of Na-insertion mechanism. It is obvious that no any monoclinic O′3 or P′3 phase can be detected for the entire electrochemical structure evolution of $NaFe_{0.3}Ni_{0.35}Mn_{0.35}O_2$, with a significant difference from $NaNi_{0.5}Mn_{0.5}O_2$.[34] The excellent structure stability is also confirmed by the ex situ XANES spectra of Ni, Fe, and Mn *K*-edges at different electrochemical states. Upon charging to 4.0 V, the Ni and Fe K-edge spectrum (Figure 4b, c) clearly shift toward a higher-energy region, showing that Na extraction is charge-compensated by the oxidation of Ni and Fe ions, demonstrated by a shift similar to previously reported results.[35,36] In contrast, the Mn *K*-edge spectrum exhibits only a change in shape attributed to the adjustment in the local coordinational structure instead of the oxidation of Mn^{4+}(Figure S6).[34] Upon discharge to 2.0 V, *K*-edge absorptions of transition metal ions shift back and overlap with that of the original sample, implying complete reversibility of the redox reaction and structure evolution accompanied by Na insertion/deinsertion.

Along with the improved cycling performance originating from the high reversibility of the structure evolution, the enhancement of the rate property is investigated by quantifying the apparent Na^+ diffusion coefficient *D* using CV analysis based on the Randles−Sevcik equation.[37] The peaks marked "1" shown in Figure 5a, b are chosen for calculations. The smaller shift of peak potential (0.54 V) with an increase in scan rates from 0.05 to 1 mV s^{-1} of $NaFe_{0.3}Ni_{0.35}Mn_{0.35}O_2$ compared to 0.68 V of $NaNi_{0.5}Mn_{0.5}O_2$ suggests the weaker polarization and faster kinetics. The linear relationship between peak current I_p and the square root of scan rate $\nu^{1/2}$ implies predominant diffusion-determining process during electrode reaction. The value of *D* for $NaFe_{0.3}Ni_{0.35}Mn_{0.35}O_2$ calculated from the slope of linear relationship is 2.81×10^{-11} cm^2 s^{-1}, a magnitude higher than 1.98×10^{-12} cm^2 s^{-1} of $NaNi_{0.5}Mn_{0.5}O_2$ (Figure 5c, d).

It is worth noting that the enhanced electron delocalization is also especially effective in enhancing air stability. The aging experiment of exposing materials to air are carried out, followed by recording the structure evolution by XRD and ABF-STEM. For $NaNi_{0.5}Mn_{0.5}O_2$, an obvious structure transition is evidenced just for 2 h of air exposure (Figure

DOI: 10.1021/acsami.9b00186
ACS Appl. Mater. Interfaces XXXX, XXX, XXX−XXX

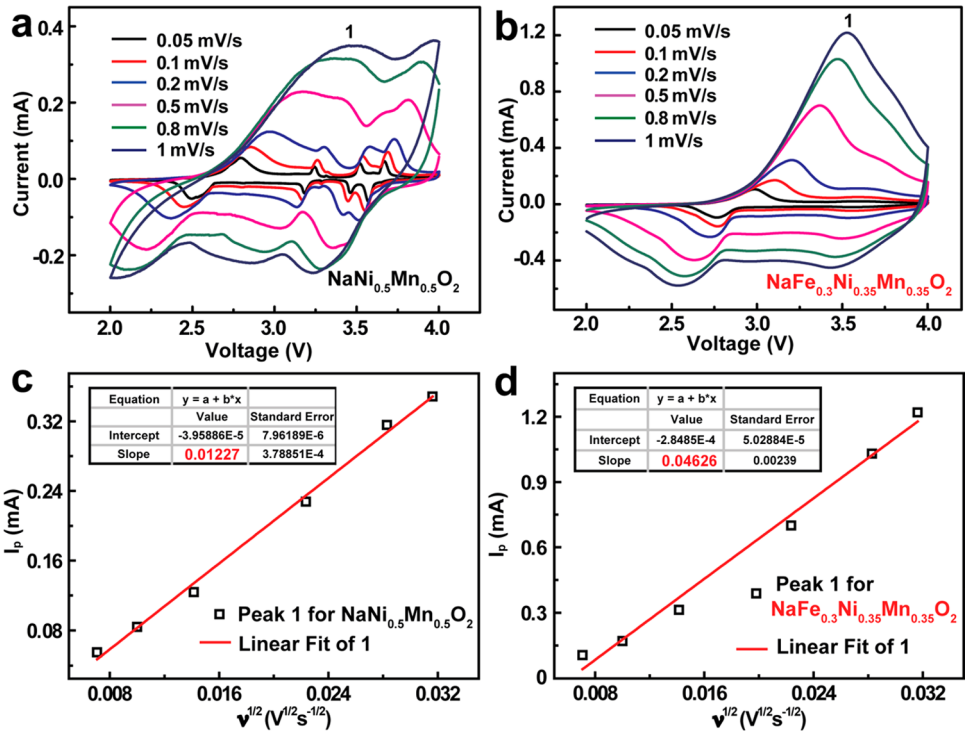

Figure 5. CV profiles of (a) $NaNi_{0.5}Mn_{0.5}O_2$ and (b) $NaFe_{0.3}Ni_{0.35}Mn_{0.35}O_2$ cathode under various scanning rates. Linear fitting of peak currents I_p by $a+bv^{1/2}$ function for (c) $NaNi_{0.5}Mn_{0.5}O_2$ and (d) $NaFe_{0.3}Ni_{0.35}Mn_{0.35}O_2$.

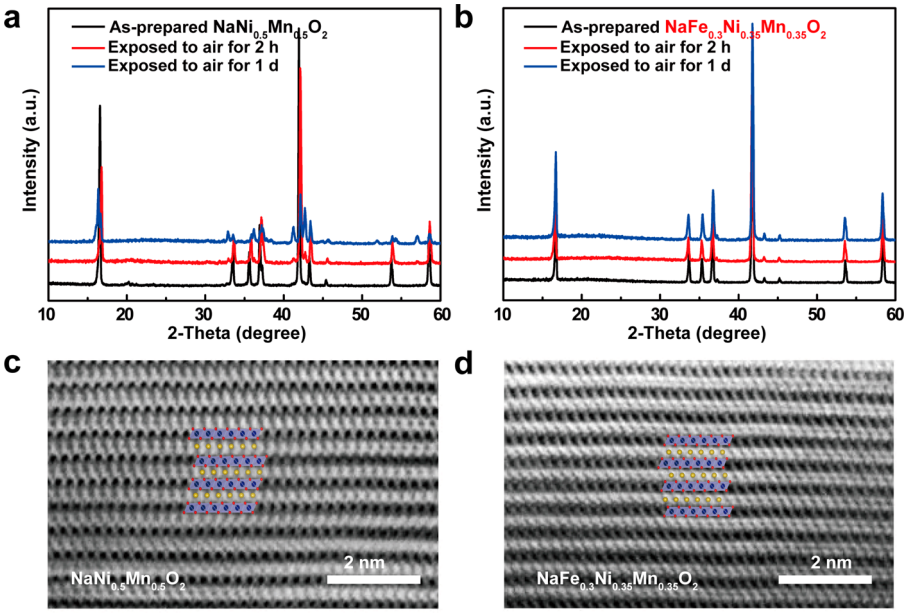

Figure 6. Comparison of XRD patterns of prepared and air-exposed (a) $NaNi_{0.5}Mn_{0.5}O_2$ and (b) $NaFe_{0.3}Ni_{0.35}Mn_{0.35}O_2$. ABF-STEM images of (c) $NaNi_{0.5}Mn_{0.5}O_2$ and (d) $NaFe_{0.3}Ni_{0.35}Mn_{0.35}O_2$ after exposed to air for 1 day.

6a), whereas no clear structure change is observed after exposed $NaFe_{0.3}Ni_{0.35}Mn_{0.35}O_2$ to air for 1 day (Figure 6b). Identified directly at atomic-scale by ABF-STEM, aged $NaNi_{0.5}Mn_{0.5}O_2$ exhibits the P3 phase verified by the prismatic coordinated Na sites and head-to-head stacking model of O columns (Figure 6c). In contrast, aged $NaFe_{0.3}Ni_{0.35}Mn_{0.35}O_2$ (Figure 6d), characterized by octahedral Na sites and ABCABC stacking O columns, remains pristine O3 phase.

In summary, an effective structure modulation strategy based on the enhancement of electron delocalization is presented to suppress monoclinic phase transitions and improve electrochemical performances and air stability. On the basis of DFT calculations and the relationship between crystal and electronic structure, Fe^{3+} with a slightly large radius is introduced into the transition metal layers of $NaNi_{0.5}Mn_{0.5}O_2$ to realize the strategy. The complete suppression of monoclinic phase transitions and high reversibility of structural evolution upon sodiation/desodiation is demonstrated by in situ XRD and ex situ XANES tests. In addition, the obtained $NaFe_{0.3}Ni_{0.35}Mn_{0.35}O_2$ shows twice the capacity retention and

DOI: 10.1021/acsami.9b00186
ACS Appl. Mater. Interfaces XXXX, XXX, XXX−XXX

10 times longer stable air-exposing time than the original $NaNi_{0.5}Mn_{0.5}O_2$, directly verified by atomic-scale ABF-STEM for the first time. The simple strategy is proved to be effective on the improvement of Na- and air-storage performances of O3-type layered oxides and opens a new avenue for designing high-performance cathode materials for the next generation energy storage devices.

■ ASSOCIATED CONTENT

Supporting Information

The Supporting Information is available free of charge on the ACS Publications website at DOI: 10.1021/acsami.9b00186.

Calculated crystal structures, SEM images and EDS analysis, XANES data at the Mn *K*-edge of $Na-Fe_{0.3}Ni_{0.35}Mn_{0.35}O_2$ recorded under various electrochemical states, and refined crystallographic parameters (PDF)

■ AUTHOR INFORMATION

Corresponding Authors

*E-mail: ygguo@iccas.ac.cn (Y.-G.G.).
*E-mail: zghuang@fjnu.edu.cn (Z.-G.H.).

ORCID

Ya-Xia Yin: 0000-0002-0983-9916
Xiong-Wei Wu: 0000-0001-9393-7123
Xiqian Yu: 0000-0001-8513-518X
Lin Gu: 0000-0002-7504-031X
Zhigao Huang: 0000-0002-8157-3550
Yu-Guo Guo: 0000-0003-0322-8476

Notes

The authors declare no competing financial interest.

■ ACKNOWLEDGMENTS

This work was supported by Basic Science Center Project of the National Natural Science Foundation of China under Grant 51788104, the National Natural Science Foundation of China (Grants 21805038, 51772301, and 21805105), the National Key R&D Program of China (Grant 2016YFA0202500).

■ REFERENCES

(1) Wang, D.; Xu, T.; Li, Y.; Pan, D.; Lu, X.; Hu, Y.-S.; Dai, S.; Bai, Y. Integrated Surface Functionalization of Li-Rich Cathode Materials for Li-Ion Batteries. *ACS Appl. Mater. Interfaces* **2018**, *10*, 41802−41813.

(2) Lee, J.; Kitchaev, D. A.; Kwon, D.-H.; Lee, C.-W.; Papp, J. K.; Liu, Y.-S.; Lun, Z.; Clément, R. J.; Shi, T.; McCloskey, B. D.; Guo, J.; Balasubramanian, M.; Ceder, G. Reversible Mn^{2+}/Mn^{4+} Double Redox in Lithium-Excess Cathode Materials. *Nature* **2018**, *556*, 185−190.

(3) Longo, R. C.; Liang, C.; Kong, F.; Cho, K. Core−Shell Nanocomposites for Improving the Structural Stability of Li-Rich Layered Oxide Cathode Materials for Li-Ion Batteries. *ACS Appl. Mater. Interfaces* **2018**, *10*, 19226−19234.

(4) Han, X.; Gong, Y.; Fu, K.; He, X.; Hitz, G. T.; Dai, J.; Pearse, A.; Liu, B.; Wang, H.; Rubloff, G.; Mo, Y.; Thangadurai, V.; Wachsman, E. D.; Hu, L. Negating Interfacial Impedance in Garnet-Based Solid-State Li Metal Batteries. *Nat. Mater.* **2017**, *16*, 572−579.

(5) Zhu, H.; Lee, K. T.; Hitz, G. T.; Han, X.; Li, Y.; Wan, J.; Lacey, S.; Cresce, A. v. W.; Xu, K.; Wachsman, E.; Hu, L. Free-Standing $Na_{2/3}Fe_{1/2}Mn_{1/2}O_2$@Graphene Film for a Sodium-Ion Battery Cathode. *ACS Appl. Mater. Interfaces* **2014**, *6*, 4242−4247.

(6) Zhang, Z.; Chen, B.; Xu, H.; Cui, Z.; Dong, S.; Du, A.; Ma, J.; Wang, Q.; Zhou, X.; Cui, G. Self-Established Rapid Magnesiation/De-Magnesiation Pathways in Binary Selenium−Copper Mixtures with Significantly Enhanced Mg-Ion Storage Reversibility. *Adv. Funct. Mater.* **2018**, *28*, 1701718.

(7) Chen, C.; Han, B.; Lin, G.; Huang, Q.; Zhao, S.; Zhang, D.; Ma, C.; Ivey, D. G.; Wei, W. Electrochemical Property−Structure Correlation for Ni-Based Layered Na-Ion Cathodes. *ACS Appl. Mater. Interfaces* **2018**, *10*, 28719−28725.

(8) Zhao, J.; Sonigara, K. K.; Li, J.; Zhang, J.; Chen, B.; Zhang, J.; Soni, S. S.; Zhou, X.; Cui, G.; Chen, L. A Smart Flexible Zinc Battery with Cooling Recovery Ability. *Angew. Chem., Int. Ed.* **2017**, *56*, 7871−7875.

(9) Maletti, S.; Giebeler, L.; Oswald, S.; Tsirlin, A. A.; Senyshyn, A.; Michaelis, A.; Mikhailova, D. Irreversible Made Reversible: Increasing the Electrochemical Capacity by Understanding the Structural Transformations of $Na_xCo_{0.5}Ti_{0.5}O_2$. *ACS Appl. Mater. Interfaces* **2018**, *10*, 36108−36119.

(10) Huang, Y.; Zheng, Y.; Li, X.; Adams, F.; Luo, W.; Huang, Y.; Hu, L. Electrode Materials of Sodium-Ion Batteries toward Practical Application. *ACS Energy Lett.* **2018**, *3*, 1604−1612.

(11) Chou, S.; Yu, Y. Next Generation Batteries: Aim for the Future. *Adv. Energy Mater.* **2017**, *7*, 1703223.

(12) Wu, C.; Dou, S.-X.; Yu, Y. The State and Challenges of Anode Materials Based on Conversion Reactions for Sodium Storage. *Small* **2018**, *14*, No. e1703671.

(13) Shen, F.; Luo, W.; Dai, J.; Yao, Y.; Zhu, M.; Hitz, E.; Tang, Y.; Chen, Y.; Sprenkle, V. L.; Li, X.; Hu, L. Ultra-Thick, Low-Tortuosity, and Mesoporous Wood Carbon Anode for High-Performance Sodium-Ion Batteries. *Adv. Energy Mater.* **2016**, *6*, 1600377.

(14) Kundu, D.; Talaie, E.; Duffort, V.; Nazar, L. F. The Emerging Chemistry of Sodium Ion Batteries for Electrochemical Energy Storage. *Angew. Chem., Int. Ed.* **2015**, *54*, 3431−3448.

(15) Pan, H.; Hu, Y.-S.; Chen, L. Room-Temperature Stationary Sodium-Ion Batteries for Large-Scale Electric Energy Storage. *Energy Environ. Sci.* **2013**, *6*, 2338−2360.

(16) Guo, S.; Yi, J.; Sun, Y.; Zhou, H. Recent Advances in Titanium-Based Electrode Materials for Stationary Sodium-Ion Batteries. *Energy Environ. Sci.* **2016**, *9*, 2978−3006.

(17) Chen, T.-R.; Sheng, T.; Wu, Z.-G.; Li, J.-T.; Wang, E.-H.; Wu, C.-J.; Li, H.-T.; Guo, X.-D.; Zhong, B.-H.; Huang, L.; Sun, S.-G. Cu^{2+} Dual-Doped Layer-Tunnel Hybrid $Na_{0.6}Mn_{1-X}Cu_xO_2$ as a Cathode of Sodium-Ion Battery with Enhanced Structure Stability, Electrochemical Property, and Air Stability. *ACS Appl. Mater. Interfaces* **2018**, *10*, 10147−10156.

(18) Lee, E.; Lu, J.; Ren, Y.; Luo, X.; Zhang, X.; Wen, J.; Miller, D.; DeWahl, A.; Hackney, S.; Key, B.; Kim, D.; Slater, M. D.; Johnson, C. S. Layered P2/O3 Intergrowth Cathode: Toward High Power Na-Ion Batteries. *Adv. Energy Mater.* **2014**, *4*, 1400458.

(19) Yabuuchi, N.; Kubota, K.; Dahbi, M.; Komaba, S. Research Development on Sodium-Ion Batteries. *Chem. Rev.* **2014**, *114*, 11636−11682.

(20) Li, X.; Ma, X.; Su, D.; Liu, L.; Chisnell, R.; Ong, S. P.; Chen, H.; Toumar, A.; Idrobo, J.-C.; Lei, Y.; Bai, J.; Wang, F.; Lynn, J. W.; Lee, Y. S.; Ceder, G. Direct Visualization of the Jahn−Teller Effect Coupled to Na Ordering in $Na_{5/8}MnO_2$. *Nat. Mater.* **2014**, *13*, 586−592.

(21) Vassilaras, P.; Ma, X.; Li, X.; Ceder, G. Electrochemical Properties of Monoclinic $NaNiO_2$. *J. Electrochem. Soc.* **2013**, *160*, A207−A211.

(22) Han, M. H.; Gonzalo, E.; Casas-Cabanas, M.; Rojo, T. Structural Evolution and Electrochemistry of Monoclinic $NaNiO_2$ Upon the First Cycling Process. *J. Power Sources* **2014**, *258*, 266−271.

(23) Bai, L.; Zhang, Y.; Zhang, L.; Zhang, Y.; Sun, L.; Ji, N.; Li, X.; Si, H.; Zhang, Y.; Huang, H. Jahn-Teller Distortions in Molybdenum Oxides: An Achievement in Exploring High Rate Supercapacitor Applications and Robust Photocatalytic Potential. *Nano Energy* **2018**, *53*, 982−992.

DOI: 10.1021/acsami.9b00186
ACS Appl. Mater. Interfaces XXXX, XXX, XXX−XXX

(24) Prasad, R.; Benedek, R.; Thackeray, M. M. Dopant-Induced Stabilization of Rhombohedral $Limno_2$ against Jahn-Teller Distortion. *Phys. Rev. B: Condens. Matter Mater. Phys.* **2005**, *71*, 134111.
(25) Clement, R. J.; Billaud, J.; Robert Armstrong, A.; Singh, G.; Rojo, T.; Bruce, P. G.; Grey, C. P. Structurally Stable Mg-Doped P2-$Na_{2/3}Mn_{1-Y}Mg_yO_2$ Sodium-Ion Battery Cathodes with High Rate Performance: Insights from Electrochemical, Nmr and Diffraction Studies. *Energy Environ. Sci.* **2016**, *9*, 3240−3251.
(26) Xiao, B.; Sun, X. Surface and Subsurface Reactions of Lithium Transition Metal Oxide Cathode Materials: An Overview of the Fundamental Origins and Remedying Approaches. *Adv. Energy Mater.* **2018**, *8*, 1802057.
(27) Yuan, D. D.; Wang, Y. X.; Cao, Y. L.; Ai, X. P.; Yang, H. X. Improved Electrochemical Performance of Fe-Substituted Na-$ni_{0.5}Mn_{0.5}O_2$ Cathode Materials for Sodium-Ion Batteries. *ACS Appl. Mater. Interfaces* **2015**, *7*, 8585−8591.
(28) Bianchini, F.; Fjellvag, H.; Vajeeston, P. A First Principle Comparative Study of the Ionic Diffusivity in $LiAlO_2$ and $NaAlO_2$ Polymorphs for Solid-State Battery Applications. *Phys. Chem. Chem. Phys.* **2018**, *20*, 9824−9832.
(29) Liu, Y.; Wang, C.; Kong, X.; Duan, D. Stability and Superconductivity of K−P Compounds under Pressure. *Inorg. Chem.* **2017**, *56*, 12529−12534.
(30) Li, Y.; Jin, X.; Cui, T.; Zhuang, Q.; Lv, Q.; Wu, G.; Meng, X.; Bao, K.; Liu, B.; Zhou, Q. Structural Stability and Electronic Property in K_2S under Pressure. *RSC Adv.* **2017**, *7*, 7424−7430.
(31) You, Y.; Xin, S.; Asl, H. Y.; Li, W.; Wang, P.-F.; Guo, Y.-G.; Manthiram, A. Insights into the Improved High-Voltage Performance of Li-Incorporated Layered Oxide Cathodes for Sodium-Ion Batteries. *Chem.* **2018**, *4*, 2124−2139.
(32) Yao, H.-R.; Wang, P.-F.; Gong, Y.; Zhang, J.; Yu, X.; Gu, L.; OuYang, C.; Yin, Y.-X.; Hu, E.; Yang, X.-Q.; Stavitski, E.; Guo, Y.-G.; Wan, L.-J. Designing Air-Stable O3-Type Cathode Materials by Combined Structure Modulation for Na-Ion Batteries. *J. Am. Chem. Soc.* **2017**, *139*, 8440−8443.
(33) Wang, P.-F.; You, Y.; Yin, Y.-X.; Guo, Y.-G. An O3-Type $NaNi_{0.5}Mn_{0.5}O_2$ Cathode for Sodium-Ion Batteries with Improved Rate Performance and Cycling Stability. *J. Mater. Chem. A* **2016**, *4*, 17660−17664.
(34) Komaba, S.; Yabuuchi, N.; Nakayama, T.; Ogata, A.; Ishikawa, T.; Nakai, I. Study on the Reversible Electrode Reaction of $Na_{1-X}Ni_{0.5}Mn_{0.5}O_2$ for a Rechargeable Sodium-Ion Battery. *Inorg. Chem.* **2012**, *51*, 6211−6220.
(35) Yoon, W.-S.; Paik, Y.; Yang, X.-Q.; Balasubramanian, M.; McBreen, J.; Grey, C. P. Investigation of the Local Structure of the $Lini_{0.5}mn_{0.5}o_2$ Cathode Material During Electrochemical Cycling by X-Ray Absorption and Nmr Spectroscopy. *Electrochem. Solid-State Lett.* **2002**, *5*, A263−A266.
(36) Kubota, K.; Asari, T.; Yoshida, H.; Yaabuuchi, N.; Shiiba, H.; Nakayama, M.; Komaba, S. Understanding the Structural Evolution and Redox Mechanism of a $NaFeO_2$−$NaCoO_2$ Solid Solution for Sodium-Ion Batteries. *Adv. Funct. Mater.* **2016**, *26*, 6047−6059.
(37) Yao, H.-R.; Wang, P.-F.; Wang, Y.; Yu, X.; Yin, Y.-X.; Guo, Y.-G. Excellent Comprehensive Performance of Na-Based Layered Oxide Benefiting from the Synergetic Contributions of Multimetal Ions. *Adv. Energy Mater.* **2017**, *7*, 1700189.

DOI: 10.1021/acsami.9b00186
ACS Appl. Mater. Interfaces XXXX, XXX, XXX−XXX